

# On the physical nature of globular cluster candidates in the Milky Way bulge

A.E. Piatti<sup>1,2\*</sup>

<sup>1</sup> Consejo Nacional de Investigaciones Científicas y Técnicas, Av. Rivadavia 1917, C1033AAJ, Buenos Aires, Argentina

<sup>2</sup> Observatorio Astronómico, Universidad Nacional de Córdoba, Laprida 854, 5000, Córdoba, Argentina

Accepted XXX. Received YYY; in original form ZZZ

## ABSTRACT

We present results from 2MASS  $JK_s$  photometry on the physical reality of recently reported globular cluster (GC) candidates in the Milky Way (MW) bulge. We relied our analysis on photometric membership probabilities that allowed us to distinguish real stellar aggregates from the composite field star population. When building colour-magnitude diagrams and stellar density maps for stars at different membership probability levels, the genuine GC candidate populations are clearly highlighted. We then used the tip of the red giant branch (RGB) as distance estimator, resulting heliocentric distances that place many of the objects in regions near of the MW bulge where no GC had been previously recognised. Some few GC candidates resulted to be MW halo/disc objects. Metallicities estimated from the standard RGB method are in agreement with the values expected according to the position of the GC candidates in the Galaxy. Finally, we derived from the first time their structural parameters. We found that the studied objects have core, half-light and tidal radii in the ranges spanned by the population of known MW GCs. Their internal dynamical evolutionary stages will be described properly when their masses are estimated.

**Key words:** techniques: photometric – galaxies: individual: Milky Way – galaxies: star clusters: general

## 1 INTRODUCTION

Recently, Minniti et al. (2017, hereafter M17) have reported 22 new globular cluster (GC) candidates from overdensities in red giant branch (RGB) star maps built from photometric data sets of the VISTA<sup>1</sup> Variables in the Vía Láctea (VVV) survey (Minniti et al. 2010; Saito et al. 2012). These candidates are projected in direction towards the Milky Way (MW) bulge ( $10^\circ \leq l \leq 350^\circ$ ) and were assumed to be as old as the ancient MW GCs. However, main sequence turnoffs of theoretical isochrones for an age of  $\log(t \text{ yr}^{-1}) = 10.1$  (12.6 Gyr) overplotted on the GC colour-magnitude diagrams (CMDs) constructed by M17 (see their figure 3) are  $\sim 0.5$ -1.5 mag fainter than the observed ones. We checked these values by first snapping 12 M17's CMDs with clear GC sequences (#3, 5, 6, 8, 15, 16, 17, 18, 19, 20, 21, 22), then overplotted the respective Bressan et al. (2012)'s isochrones using PYTHON tools and finally estimated them by visual inspection. The isochrones for the metallicities of the corresponding reference GCs assigned by M17 were previously

shifted by reddening and distance using the values obtained by them (their table 1). Indeed, the main sequence turnoffs of the well-known GCs NGC 6637 and 6642, also included in their CMDs sample, are fainter than the limiting magnitude reached by the VVV survey. At this point, it results also a little bit curious that most of the star field decontaminated CMDs present well-isolated main sequences turnoffs in comparison with the upper part of these CMDs, where residual stars outside the RGBs are seen.

Such mismatches trigger the unavoidable question about the reliability of the distance estimates for these GC candidates, the assumption of ages similar to those of old MW bulge GCs, and even about the real nature of such RGB star overdensities, among others. M17 estimated GC candidate distances by comparing the position of the red clump in their CMDs with those of six old known MW GCs also observed by the VVV survey. GC candidates with clear red clumps were considered metal-rich ( $[\text{Fe}/\text{H}] > -1$  dex) objects, while those without prominent ones were treated as metal-poor ( $[\text{Fe}/\text{H}] < -1$  dex) candidates. Such a distinction was necessary to select the reference MW GCs to which measure the difference in red clump magnitudes. M17 men-

\* E-mail: andres@oac.unc.edu.ar

<sup>1</sup> Visible and Infrared Survey Telescope for Astronomy

tioned that, if they were real GCs, they should be grouped more or less symmetrically around the Galactic centre.

We here embarked in a thorough study aiming at confirming the physical nature of these objects from independent data sets and analysis approaches. We relied on the extensive use of the tip of the red giant branch (RGBT) to determine extragalactic distances (see, e.g., [Serenelli et al. 2017](#); [Madore et al. 2018](#); [Hoyt et al. 2018](#), and references therein), to estimate the GC candidate distances making use the 2MASS database ([Skrutskie et al. 2006](#)). While the VVV photometry saturates for magnitudes brighter than  $K_s \sim 12.0$  mag, the 2MASS one is able to reach well above the RGBT of MW bulge GCs ( $K_s \sim 8.0$  mag, [Cohen et al. 2015](#)). Therefore, from 2MASS photometry is possible to trace the upper part of the RGBs of the M17's GC candidates, and by employing the magnitude of the RGBT to estimate reliable distances ([Müller et al. 2018](#); [Sabbi et al. 2018](#); [Beaton & Carnegie-Chicago Hubble Program Team 2018](#)). It is worth mentioning that 2MASS data have been extensively used in the last decades to search for new GCs (see, e.g., [Hurt et al. 2000](#); [Ivanov et al. 2000, 2002](#); [Borissova et al. 2003](#); [Froeblich et al. 2007](#); [Bica et al. 2007](#); [Bonatto et al. 2007](#); [Strader & Koblunicky 2008](#); [Scholz et al. 2015](#)).

In Section 2 we describe the procedure applied to assign membership probabilities to stars observed in the GC candidate fields, the technique to estimate their metal content, and the methods for constructing their stellar radial profiles and estimating their structural parameters. In Section 3, we discuss the results to the light of our previous knowledge of the MW bulge GC population and those of M17. Particularly, we compared the derived structural parameters (core, half-light, tidal radii) with those compiled by [Harris \(1996\)](#) and our distance estimates with those derived by M17. Finally, in Section 4 we summarize the main conclusions of this work.

## 2 DATA HANDLING

We downloaded 2MASS  $JK_s$  data sets from the IPAC Infrared Science Archive<sup>2</sup> (IRSA) for circular regions with radii of 30 arcmin around the GC candidate centres. Such regions pretty well cover the whole objects extensions and their surrounding fields. Indeed, the six MW GCs used as reference by M17 have radii between  $\sim 4 - 7$  arcmin ([Harris 1996](#)), while M17 estimated sizes of  $\sim 2 - 5$  arcmin in radius for their 22 GC candidates.

We first defined a circular region with a radius of 10 arcmin around each GC candidate centre and eight additional circular regions of that same size, uniformly distributed around its centre, at a distance of 20 arcmin. For the eight GC candidate surrounding regions, we built their respective  $K_s$  versus  $J - K_s$  CMDs and produced a collection of rectangular cells centred at the position of each star and with dimensions - defined independently for magnitude and colour - in such a way that there is no star inside each cell but that at its centre, with the following closest one located at one of the four corners of the rectangular cell. This array of cells properly reproduces the stellar density of

that surrounding field and appropriately traces its luminosity function and colour distribution in the CMD. We refer to the works by [Piatti et al. \(2018\)](#), among others, where the reader will find illustrations about the generation of the rectangular cells. The method was developed by [Piatti & Bica \(2012\)](#) with the aim of providing a robust approach to statistically clean the CMDs from the field star contamination. We have used it since then dealing with optical and near-infrared photometries of MW and Magellanic Clouds star clusters in crowded and highly reddened stars fields (see, e.g. [Piatti & Cole 2017](#)).

Each collection of cells per surrounding field CMD was superimposed on the GC candidate CMD, and then subtracted from it one star per defined cell: the closest one to the cells' centres. Thus we cleaned the GC candidates CMDs by eliminating the same number of stars as in the surrounding field CMD, according to the particular pattern along the magnitude and colour ranges of that surrounding field. Since we repeated this exercise eight times - one per surrounding field CMD -, we generated eight different cleaned GC candidate CMDs. We then combined all of them by producing a master GC candidate cleaned CMD where we assigned to each star a statistical photometric membership status. Stars that were kept unsubtracted eight times have a membership probability  $P = 100\%$ ; those stars left in the master cleaned CMD seven times, a  $P$  value of 88%; stars six times unsubtracted have  $P = 75\%$ , and so forth, until  $P = 13\%$  for those stars that appear once in the master cleaned CMD. Thus, we were able to recognise stellar populations that most probably belong to the field - those having the smallest  $P$  values -, i.e., stars that are more or less similarly distributed as a function of stellar density, luminosity function and colour distribution throughout the GC candidate field; and stars that represent a local intrinsic feature of that part of the sky - stars with the largest  $P$  values -. These stars could be part of a star cluster or of an apparent enhancement of stars along that line-of-sight. Stars with  $P = 50\%$  can be either part of the composite field population or belong to the local stellar enhancement. Fig. 1 depicts some resulting CMDs of Minni 16 for different membership probabilities. CMDs for smaller  $P$  values ( $P = 38, 25$  and  $13\%$ ) are less worth for our study, since they show repeatedly the composite field population. As can be seen, the broadnesses of the RGBs become narrower as the CMDs are built with larger  $P$  values, suggesting the transition from a composite field stellar population to that of a stellar aggregate.

[Serenelli et al. \(2017\)](#) have comprehensively studied the characteristics of the RGBT from a theoretical point of view and provided a set of relationships to compute the absolute  $K_s$  magnitude of the RGBT ( $M_{K_s}^{RGBT}$ ) in terms of the intrinsic  $(J - K_s)_o$  colour (not affected by reddening). We took advantage of these relationships to estimate the GC candidate distances. We first measured the observed  $K_s$  magnitudes and  $J - K_s$  colours of the RGBT in the GC candidate cleaned CMDs; then we corrected them by reddening effect using the  $E(J - K_s)$  values in M17 and the relation  $A_{K_s} = 0.428E(J - K_s)$  ([Alonso-García et al. 2015](#)). Finally, we computed the  $M_{K_s}^{RGBT}$  absolute magnitudes from the dereddened  $(J - K_s)_o$  colours and the equations of [Serenelli et al. \(2017](#), see their table 1), and the absolute distance moduli using these latter values and the dereddened  $K_s$  magnitudes. Because CMDs for  $P = 88\%$  and  $100\%$  exhibit

<sup>2</sup> [www.ipac.caltech.edu/2mass/overview/access.html](http://www.ipac.caltech.edu/2mass/overview/access.html)

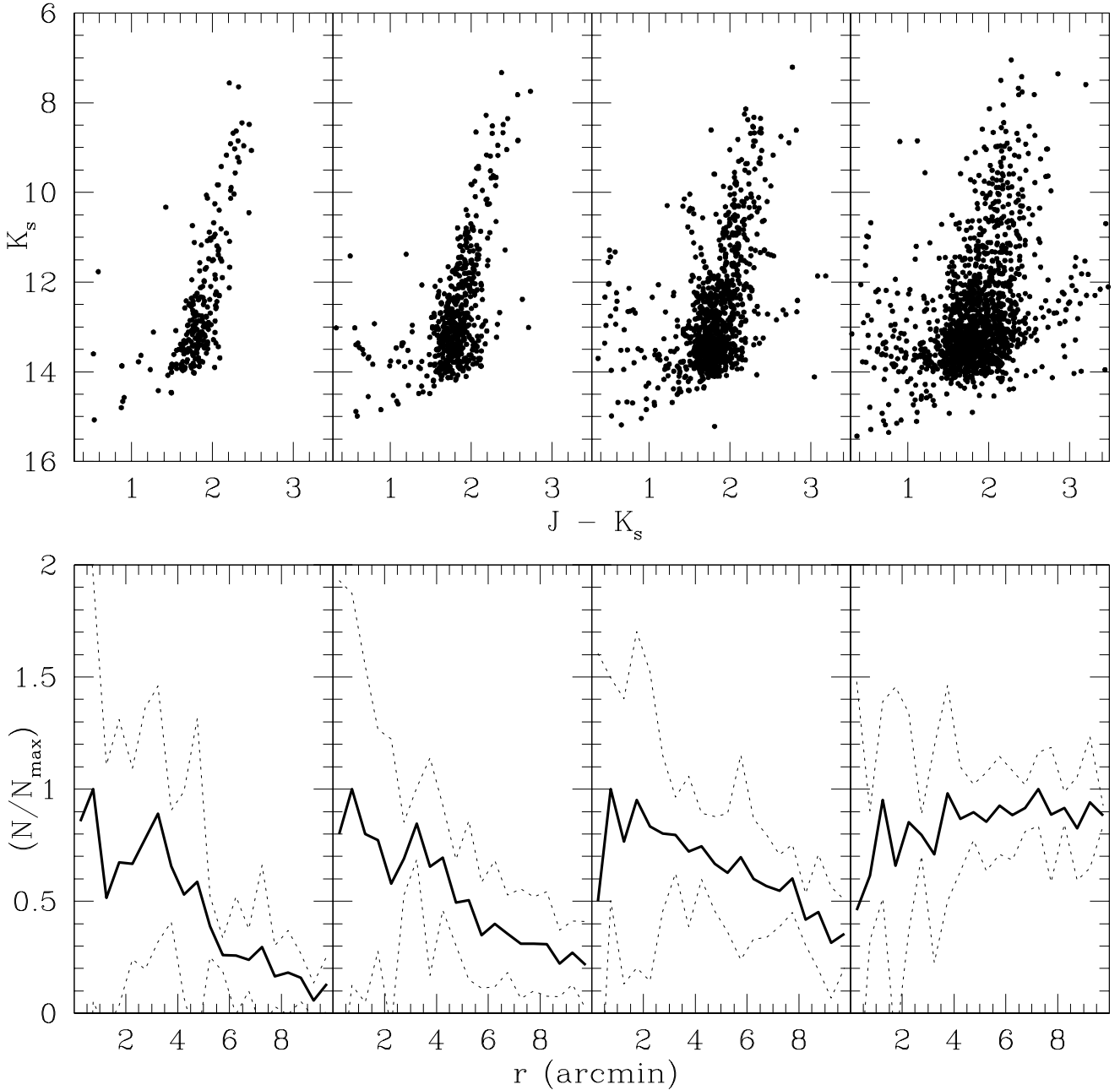


**Figure 1.** *Top:*  $K_s$  versus  $J - K_s$  CMDs for stars distributed in the field of Minni 16 for membership probabilities  $P = 100, 88, 75$  and  $50\%$  (from left to right), respectively. *Bottom:* Observed stellar radial profiles for the above respective  $P$  values. The solid and dotted lines represent the average and standard deviation. Similar figures for the remaining 21 GC candidates are provided as supplementary material in the online version of the journal.

narrower RGBs respect to CMDs of smaller  $P$  values, we used both of them to measure  $K_s$  magnitudes and  $J - K_s$  colours of the RGBTs. We built the  $K_s$  luminosity function of the RGB using bins of 0.1 mag wide and then identified by visual inspection its sudden truncation, as well as the corresponding  $J - K_s$  colour. In some few cases we also used the  $P = 75\%$  CMDs. We estimated errors of  $\sigma(K_s^{RGBT}) = 0.15$  mag and  $\sigma((J - K_s)^{RGBT}) = 0.05$  mag, respectively, to which we added the uncertainties in  $E(J - K_s)$

( $\sigma E(J - K_s) = 0.05$  mag) to calculate errors in their dereddened values. Table 1 lists the measured  $K_s^{RGBT}$  magnitudes and  $(J - K_s)^{RGBT}$  colours and the resulting distances. As an external check, we repeated this procedure to estimate the distance of NGC 6637. We used 2MASS  $JK_s$  photometry, cleaned its CMD and measured the magnitude and the colour of its RGBT and obtained the same value provided by Harris (1996) within 0.2 kpc.

The slope of GC RGBs has been found to be related

**Table 1.** Derived properties of studied GC candidates.

ID	$(J - K_s)^{RGBT}$ (mag)	$K_s^{RGBT}$ (mag)	$d$ (kpc)	[Fe/H] (dex)	$r_c$ (pc)	$r_h$ (pc)	$r_t$ (pc)	Class
Minni 1	1.10	10.00	$16.2 \pm 3.0$ 8.1	-1.2	$0.9 \pm 0.5$ $0.5 \pm 0.2$	$5.7 \pm 1.4$ $2.8 \pm 0.7$	$47.1 \pm 14.1$ $23.6 \pm 7.1$	disc/halo
Minni 2	1.15	10.80	$24.2 \pm 4.5$ 6.6	-1.5	$1.4 \pm 0.7$ $0.4 \pm 0.2$	$8.4 \pm 2.1$ $2.3 \pm 0.6$	$70.4 \pm 21.1$ $19.2 \pm 5.8$	disc/halo
Minni 3	0.90	12.20	$38.1 \pm 6.7$ 7.0	-2.0	$2.2 \pm 1.1$ $0.4 \pm 0.2$	$13.3 \pm 3.3$ $2.4 \pm 0.6$	$110.8 \pm 33.2$ $20.4 \pm 6.1$	disc/halo
Minni 4	1.40	8.40	$9.8 \pm 1.9$ 5.3	-0.3	$0.6 \pm 0.3$ $0.3 \pm 0.2$	$3.4 \pm 0.9$ $1.9 \pm 0.5$	$28.5 \pm 8.6$ $15.4 \pm 4.6$	bulge
Minni 5	1.70	7.75	$9.8 \pm 2.1$ 8.5	-0.1	$0.6 \pm 0.3$ $0.5 \pm 0.2$	$3.4 \pm 0.9$ $3.0 \pm 0.7$	$28.5 \pm 8.6$ $24.7 \pm 7.4$	bulge
Minni 6	1.40	8.10	$8.3 \pm 1.7$ 8.4	-0.3	$0.5 \pm 0.2$ $0.5 \pm 0.2$	$2.9 \pm 0.7$ $2.9 \pm 0.7$	$24.1 \pm 7.2$ $24.4 \pm 7.3$	bulge
Minni 7	1.50	9.00	$14.0 \pm 2.8$ 6.8	-0.3	$0.8 \pm 0.4$ $0.4 \pm 0.2$	$4.9 \pm 1.2$ $2.4 \pm 0.6$	$40.7 \pm 12.2$ $19.8 \pm 5.9$	—
Minni 8	1.35	9.50	$14.7 \pm 2.8$ 7.2	-0.9	$0.9 \pm 0.4$ $0.4 \pm 0.2$	$5.1 \pm 1.3$ $2.5 \pm 0.6$	$42.8 \pm 12.8$ $20.9 \pm 6.3$	disc/halo
Minni 9	1.60	8.40	$10.3 \pm 2.1$ 8.5	-0.1	$0.6 \pm 0.3$ $0.5 \pm 0.2$	$3.6 \pm 0.9$ $3.0 \pm 0.7$	$30.0 \pm 9.0$ $24.7 \pm 7.4$	bulge
Minni 10	1.70	9.40	$15.6 \pm 3.1$ 9.5	-0.3	$0.9 \pm 0.5$ $0.6 \pm 0.3$	$5.4 \pm 1.4$ $3.3 \pm 0.8$	$45.4 \pm 13.6$ $27.6 \pm 8.3$	—
Minni 11	1.80	8.70	$11.7 \pm 2.2$ 5.9	-0.3	$0.7 \pm 0.3$ $0.3 \pm 0.2$	$4.1 \pm 1.0$ $2.1 \pm 0.5$	$34.0 \pm 10.2$ $17.2 \pm 5.1$	—
Minni 12	1.95	8.00	$8.5 \pm 1.7$ 5.6	+0.0	$0.5 \pm 0.2$ $0.3 \pm 0.2$	$3.0 \pm 0.7$ $2.0 \pm 0.5$	$24.7 \pm 7.4$ $16.3 \pm 4.9$	bulge
Minni 13	2.20	8.40	$8.4 \pm 1.6$ 6.2	-0.3	$0.5 \pm 0.2$ $0.4 \pm 0.2$	$2.9 \pm 0.7$ $2.2 \pm 0.5$	$24.4 \pm 7.3$ $18.0 \pm 5.4$	bulge
Minni 14	3.70	8.60	$11.7 \pm 2.5$ 6.3	0.0	$0.7 \pm 0.3$ $0.4 \pm 0.2$	$4.1 \pm 1.0$ $2.2 \pm 0.5$	$34.0 \pm 10.2$ $18.3 \pm 5.5$	—
Minni 15	2.40	8.50	$9.6 \pm 1.9$ 7.0	-0.3	$0.6 \pm 0.3$ $0.4 \pm 0.2$	$3.4 \pm 0.8$ $2.4 \pm 0.6$	$27.9 \pm 8.4$ $20.4 \pm 6.1$	bulge
Minni 16	2.50	8.30	$10.2 \pm 2.1$ 7.0	-0.3	$0.6 \pm 0.3$ $0.4 \pm 0.2$	$3.6 \pm 0.9$ $2.4 \pm 0.6$	$29.7 \pm 8.9$ $20.4 \pm 6.1$	bulge
Minni 17	1.35	8.50	$9.9 \pm 1.9$ 6.0	-0.3	$0.9 \pm 0.3$ $0.5 \pm 0.2$	$3.5 \pm 0.9$ $2.1 \pm 0.5$	$28.8 \pm 8.6$ $17.5 \pm 5.2$	bulge
Minni 18	2.05	8.20	$10.2 \pm 2.1$ 7.9	+0.1	$0.6 \pm 0.3$ $0.5 \pm 0.2$	$3.6 \pm 0.9$ $2.8 \pm 0.7$	$29.7 \pm 8.9$ $23.0 \pm 6.9$	bulge
Minni 19	2.20	8.10	$12.0 \pm 2.6$ 8.1	+0.1	$0.7 \pm 0.3$ $0.5 \pm 0.2$	$4.2 \pm 1.0$ $2.8 \pm 0.7$	$34.9 \pm 10.5$ $23.6 \pm 7.1$	—
Minni 20	2.45	6.90	$7.6 \pm 1.7$ 7.3	+0.2	$0.4 \pm 0.2$ $0.4 \pm 0.2$	$3.1 \pm 0.7$ $3.0 \pm 0.6$	$22.1 \pm 6.6$ $21.2 \pm 6.4$	bulge
Minni 21	1.80	8.60	$12.4 \pm 2.5$ 7.6	-0.3	$1.1 \pm 0.4$ $0.7 \pm 0.2$	$3.6 \pm 1.1$ $2.2 \pm 0.7$	$32.5 \pm 10.8$ $19.9 \pm 6.6$	—
Minni 22	2.00	8.30	$10.8 \pm 2.2$ 6.6	+0.0	$0.6 \pm 0.3$ $0.4 \pm 0.2$	$3.8 \pm 0.9$ $2.3 \pm 0.6$	$28.3 \pm 9.4$ $17.3 \pm 5.8$	bulge

Note: to convert 1 arcmin to pc, we use the following expression,  $d \sin(1/60)$ , where  $d$  is the derived heliocentric distance in pc.

to the GC metallicity (Valenti et al. 2004; Cohen et al. 2015). Indeed, at different fixed absolute magnitudes the mean colour of the RGB is different, in the sense that the brighter the fixed RGB magnitude the larger the colour. Although it is not highly sensible to metallicity changes as compared with combinations involving blue and near-infrared passbands (see, e.g. Geisler et al. 1997), we still attempted some rough estimates under the assumption that we are dealing with old GCs. To do this, we simply superimposed a subsample of theoretical isochrones computed by Bressan et al. (2012) covering the metallicity range  $-1.5 \text{ dex} \leq [\text{Fe}/\text{H}] \leq +0.6 \text{ dex}$  on the  $P=100\%+P=88\%$  CMDs, once they were corrected by distance and reddening effects. We then interpolated the  $[\text{Fe}/\text{H}]$  values for the GC RGBs at

$M_{K_s} = -5.5 \text{ mag}$ , with an estimated uncertainty of  $\sigma[\text{Fe}/\text{H}] \approx 0.2 \text{ dex}$ . Likewise, we confirmed that the observed RGBTs are in excellent agreement with the positions suggested by the theoretical isochrones. The resulting values are listed in Table 1.

## 2.1 Stellar density profiles

We built cluster radial density profiles using stars with different  $P$  values in order to confirm that the RGB stars seen in the  $P=100\%$  CMDs correspond to real stellar overdensities, and that such overdensities progressively disappear as smaller  $P$  values are used. We started by tracing annuli of 0.5 arcmin wide centred on the GC candidates, distributed

uniformly from their centres out to 10 arcmin. Each annulus was split in four equal area regions, which were used to count the number of stars placed inside them. We then averaged the four independent number of stars counted per annulus and produced an averaged observed stellar radial profile with its scatter being represented by the standard deviation. Fig. 1 illustrates some resulting normalised stellar radial profiles for different  $P$  values with their corresponding uncertainties. As can be seen, these radial profiles show that the stars with the largest  $P$  values belong to a stellar overdensity.

Although 2MASS photometry is nearly 100% complete down to  $K_s \sim 16$  mag (Skrutskie et al. 2006), it suffers from incompleteness towards the inner GC clusters regions because of crowding effects. In order to establish the actual radial dependence of the photometry incompleteness, we used the information coming from our membership probability procedure. Stars with  $P = 13\%$  and  $25\%$  should exhibit a nearly flat distribution of their observed radial profiles, because they mainly represent the composite star field. However, Fig. 2 shows that the closer to the GC candidates' centres, the smaller the number of counted stars, which is a direct evidence of crowding effect. Therefore, we used all these radial profiles to derive the mean relation  $f = 0.099r + 0.01$ , that we used to correct the  $P = 88\%$  and  $100\%$  stellar radial profiles of the 22 GC candidates for crowding effects. The correction is carried out by dividing the observed radial profile by the function  $f$ . In order to assess the reliability of such a correction, we built the stellar radial profile of NGC 6637 as described above. We then corrected the resulting observed radial profile and overplotted on it the King (1962)'s and Plummer (1911)'s models for the core ( $r_c$ ), half-light ( $r_h$ ) and tidal ( $r_t$ ) radii compiled by Harris (1996) and Vanderbeke et al. (2015). Fig. 3 confirms that the derived correction satisfactorily restored the intrinsic NGC 6637's radial profile.

We then corrected the GC candidate observed radial profiles from crowding effect, subtracted from them the respective mean background level - measured from the outermost regions of the traced profiles -, and finally we normalised them. Subsequently, we fitted King (1962)'s models from a grid of  $r_c$  and  $r_t$  values, as well as Plummer (1911)'s profiles in order to have independent estimates of the  $r_h$  radii. The  $r_c$ ,  $r_h$ , and  $r_t$  values which made both models best resembled the GC candidate intrinsic profiles were derived from  $\chi^2$  minimisation. Fig. 4 shows the normalised corrected radial profiles with the King and Plummer curves superimposed, while Table 1 lists the resulting  $r_c$ ,  $r_h$ , and  $r_t$  values with their respective uncertainties. Below our values for each GC candidate, we included the M17's distance and the corresponding radii, for comparison purposes.

### 3 ANALYSIS AND DISCUSSION

We plotted in Fig. 5 the distribution of the estimated distances in different projected MW planes. Galactic coordinates were calculated from the distances ( $d$ ) listed in Table 1 and the Galactic coordinates ( $l, b$ ) provided in M17. The  $X$ ,  $Y$ ,  $Z$  directions were chosen so that the  $X$  axis increases from the Galactic centre towards  $l = 270^\circ$ , the  $Y$  axis runs positive towards  $l = 180^\circ$  and the  $Z$  axis is perpendicular

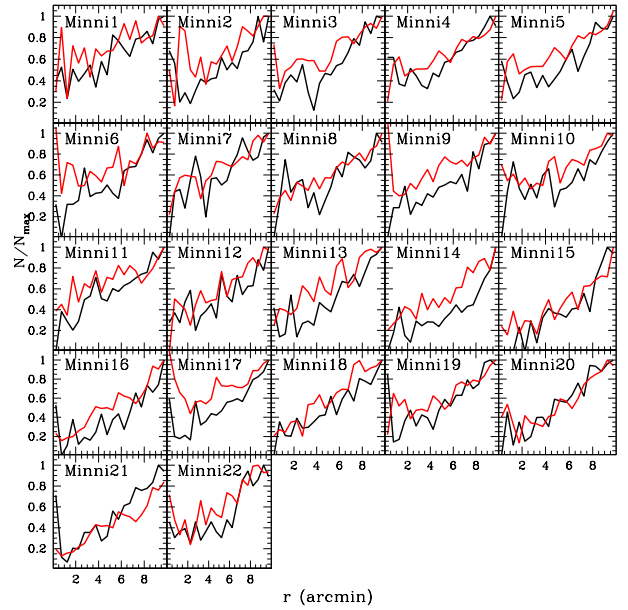


**Figure 2.** Normalised observed stellar radial profiles for stars with  $P = 13\%$  and  $25\%$  drawn with solid black and red lines, respectively, for the 22 GC candidates.

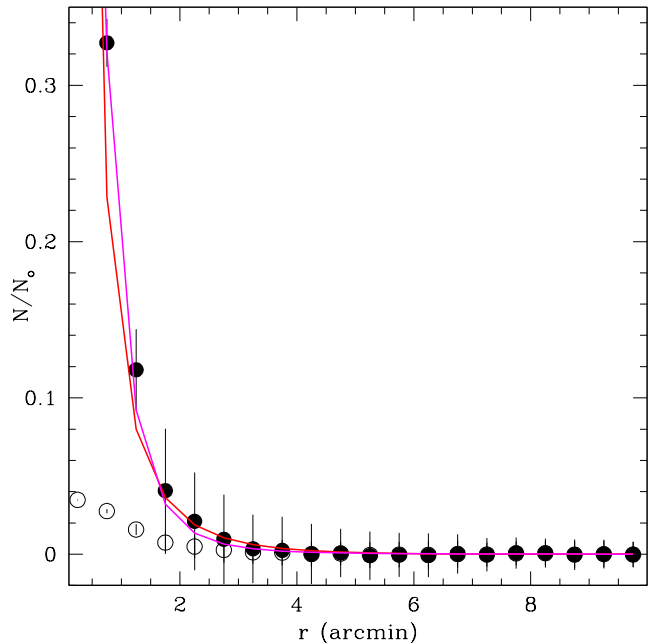


**Figure 3.** Normalised observed and corrected from crowding effect stellar radial profile of NGC 6637 depicted with open and filled circles, respectively. Both distributions are background subtracted radial profiles. Errorbars are also included. The red and magenta solid lines represent the King (1962)'s and Plummer (1911)'s models for the core, half-light and tidal radii compiled by Harris (1996) and Vanderbeke et al. (2015).

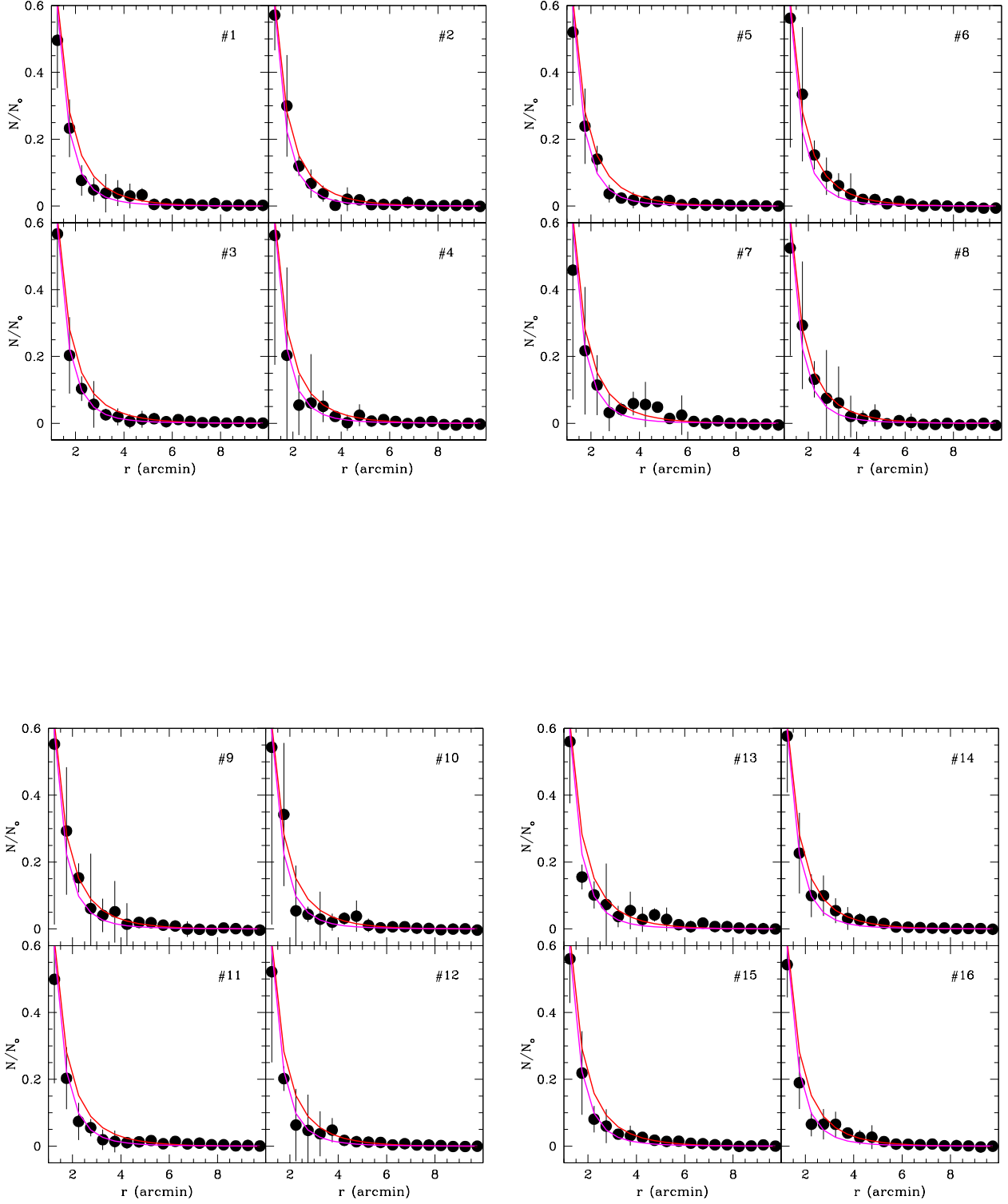


**Figure 4.** Normalised, corrected from crowding effects and background subtracted stellar radial profiles for the studied GC candidates, with their respective errorbars. Solid red and magenta lines represent the fitted King (1962)'s and Plummer (1941)'s models. MNRAS **000**, 1–9 (2017)

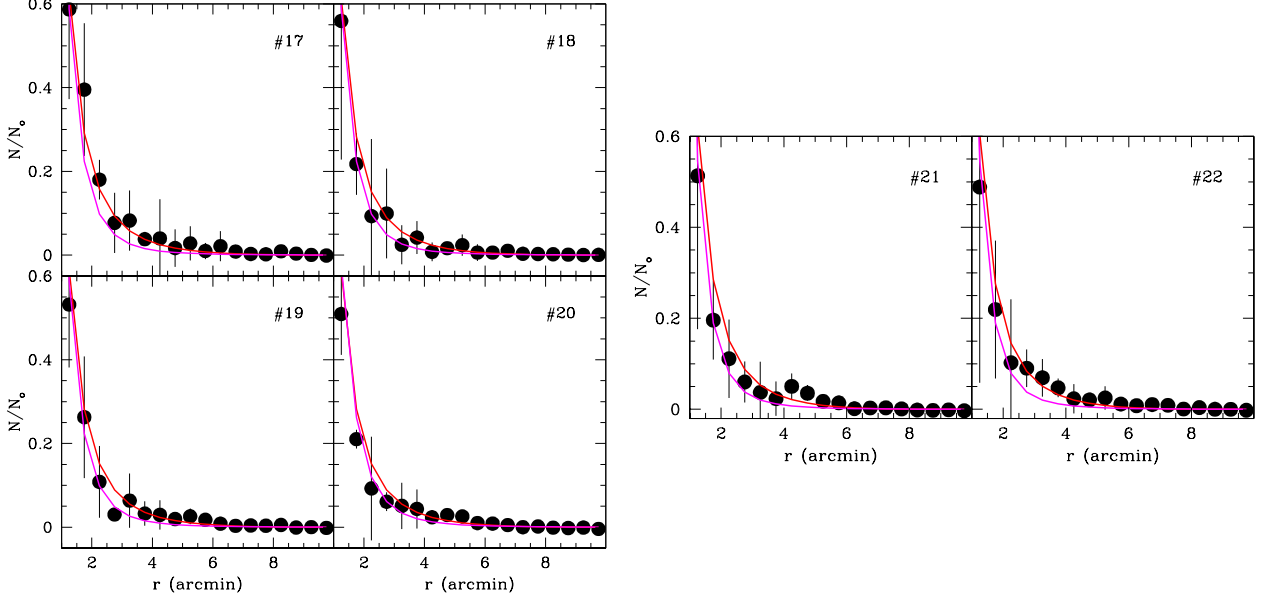


Figure 4. continued.

to the Galactic plane, pointing to the North Galactic pole. We used a Sun’s distance to the Galactic centre of 8.3 kpc (de Grijs & Bono 2017). We distinguished GC candidates more metal-poor and more metal-rich than  $[\text{Fe}/\text{H}] = -0.8$  dex with blue and red filled circles, respectively. For comparison purposes, we included the positions of known MW GCs compiled by Harris (1996) with Galactic longitudes in the same range as those for the GC candidates. They are drawn with open circles.

The different projections reveal that many GC candidates are placed in the MW bulge, occupying regions where there were not any GC catalogued previously. This is an interesting result, because these GC candidates fill other parts of the MW bulge volume, giving thus a more complete picture of their actual distribution. Note that Barros et al. (2016, and references therein) describe the MW bulge as an oblate spheroid with a radius of 3 kpc encompassing  $\sim 90$  per cent of its mass. Interestingly enough results also that some GC candidates appear to be MW halo/disc objects, as judged by their derived heliocentric distances (Minniti 1995; Côté 1999; Bica et al. 2016). Indeed, Minni 3 seems to be one of the farthest GCs to the Sun observed across the MW bulge so far.

The distinction between halo/disc and bulge GC candidates is supported by their estimated metallicities. As can be seen, MW bulge GCs are more metal-rich objects in comparison to those placed in the MW halo/disc (Minniti 1995;

Côté 1999; Bica et al. 2016). The present GC candidates spatial distribution is more consistent with their physical nature as MW bulge GCs - except those located out of the bulge - than that that comes from considering the heliocentric distances estimated by M17. Indeed, a simple comparison shows that their heliocentric distances are in average  $\sim 4$  kpc smaller than ours (see Fig. 6).

Besides Galactic positions and metallicities, structural parameters such as core, half-light and tidal radii can also help us to disentangle the physical reality of the studied objects. They can tell us about the GC candidates internal dynamical histories. For instance, some MW GCs are core-collapsed objects or clusters in a highly advanced dynamical stage. This implies that their concentration parameters  $c$  ( $\equiv \log(r_t/r_c)$ ) are within the largest possible values. This is because two-body relaxation mechanisms cause outermost cluster regions expand while the cluster core squeezes. Galactic tidal forces also play an additional role, frequently producing an extra expansion of the outermost cluster regions (see, e.g. Piatti 2017, 2018, and references therein).

We started by comparing our estimated structural parameters ( $r_c$ ,  $r_h$  and  $r_t$ ) with those of MW bulge GCs. We restricted the comparison to this particular subsample in order to facilitate the analysis with the bulge GC candidates. We assumed that if the studied bulge GC candidates are genuine bulge GCs, they should have structural parameters in the ranges spanned by already known MW bulge GCs.

Fig. 7 depicts different structural parameter relationships for them. The upper panels show that the  $r_c$ ,  $r_h$ ,  $r_t$  values of the studied bulge GC candidates are comparable with those of catalogued MW bulge GCs. In the figure we have represented studied and catalogued GCs with filled and open circles. The bulge GC candidates are drawn with red circles, while halo/disc GC candidates - included for completeness purposes - are shown with blue circles. As can be seen, there is a general superposition between the different structural parameter ranges, although the studied GC candidates tend to cover the regime with larger  $r_h$  values. It would be interesting to trace stellar radial profiles for these objects from a much higher spatial resolution photometry, in order to probe whether the incompleteness correction applied from stellar crowding effects could lead to slightly larger values, particularly in the case of  $r_h$ . As for  $r_t$ , we think that they should not be residually affected by this correction.

The bottom panels of Fig. 7 shows that the ratio between different structural parameters are in fairly good agreement with those for known MW bulge GCs. According to Harris (1996), concentration parameters close to  $c \sim 2.5$  are core-collapsed GCs. They also appear at the bottom-left corner of the  $r_c/r_h$  vs  $r_h/r_t$  plane, where a cluster moves approximately in the top-right-bottom-left direction (Heggie & Hut 2003, see, e.g., their figure 33.2) while relaxing toward a core-collapse stage. The stage of internal dynamical evolution of the studied GC candidates depend on their masses and on the MW tidal field as well. Although we could assume that MW bulge GCs have spent most of their lifetime describing small orbits around the MW centre, and therefore they have been similarly affected by the gravitational field, we would need to know their masses in order to compute half-light relaxation times. With this latter property we would be able to describe more properly their real dynamical stages. Table 1 lists in the last column the classification of the studied GC candidates on the basis of their heliocentric distances and metallicities as discussed above. We did not assign any classification to six GCs with  $[\text{Fe}/\text{H}] \geq -0.8$  dex located beyond a circle of 3 kpc from the Galactic centre, because their metallicities and heliocentric distances lead to different classifications.

#### 4 CONCLUSIONS

From 2MASS  $JK_s$  photometry we have addressed the issue about the physical entity of recently reported 22 GC candidates located towards the MW bulge, from the VVV survey. The analysis performed is twofold. On the one hand, we used different data sets, and on the other hand, the CMD features examined and the methodology employed to estimate astrophysical properties are different as well. Here we took advantage of the RGBT as a distance estimator.

We relied our analysis on an extensively applied and successful procedure to assign photometric membership probabilities to stars measured in the GC candidate field. Thus, we were able to disentangle the composite star field population from those real local stellar enhancements around the GC candidates central positions. Such stellar overdensity does not only constitute a genuine distinct group of stars projected on the observed field, but also their RGBs are remarkably well-delineated and narrower than those for

the composite star field population. Both results led us to confirm their nature as stellar aggregates.

Their estimated heliocentric distances place them behind the Galactic centre; several of them near to bulge regions where no previous GC had been identified, whereas some few other objects resulted to be MW halo/disc clusters. The distinction between MW bulge and halo/disc GC candidates is fully supported by our estimated metallicities.

We derived for the first time their structural parameters, namely: core, half-light and tidal radii. The different resulting radii suggest that these GC candidates do not differentiate from the population of known MW GCs, and particularly from those of the bulge. They are comprised within the typical bulge GC dimensions and within the expected dynamical evolutionary stages.

#### ACKNOWLEDGEMENTS

This publication makes use of data products from the Two Micron All Sky Survey, which is a joint project of the University of Massachusetts and the Infrared Processing and Analysis Center/California Institute of Technology, funded by the National Aeronautics and Space Administration and the National Science Foundation. We thank the referee for his/her thorough reading of the manuscript and timely suggestions to improve it.

#### REFERENCES

- Alonso-García J., Dékány I., Catelan M., Contreras Ramos R., Gran F., Amigo P., Leyton P., Minniti D., 2015, *AJ*, **149**, 99
- Barros D. A., Lépine J. R. D., Dias W. S., 2016, *A&A*, **593**, A108
- Beaton R. L., Carnegie-Chicago Hubble Program Team 2018, in American Astronomical Society Meeting Abstracts 231. p. 351.05
- Bica E., Bonatto C., Ortolani S., Barbuy B., 2007, *A&A*, **472**, 483
- Bica E., Ortolani S., Barbuy B., 2016, *Publ. Astron. Soc. Australia*, **33**, e028
- Bonatto C., Bica E., Ortolani S., Barbuy B., 2007, *MNRAS*, **381**, L45
- Borissova J., Pessev P., Ivanov V. D., Saviane I., Kurtev R., Ivanov G. R., 2003, *A&A*, **411**, 83
- Bressan A., Marigo P., Girardi L., Salasnich B., Dal Cero C., Rubele S., Nanni A., 2012, *MNRAS*, **427**, 127
- Cohen R. E., Hempel M., Mauro F., Geisler D., Alonso-García J., Kinemuchi K., 2015, *AJ*, **150**, 176
- Côté P., 1999, *AJ*, **118**, 406
- Froebrich D., Scholz A., Raftery C. L., 2007, *MNRAS*, **374**, 399
- Geisler D., Bica E., Dottori H., Claria J. J., Piatti A. E., Santos Jr. J. F. C., 1997, *AJ*, **114**, 1920
- Harris W. E., 1996, *AJ*, **112**, 1487
- Heggie D., Hut P., 2003, *The Gravitational Million-Body Problem: A Multidisciplinary Approach to Star Cluster Dynamics*
- Hoyt T. J., et al., 2018, preprint, ([arXiv:1803.01277](https://arxiv.org/abs/1803.01277))
- Hurt R. L., Jarrett T. H., Kirkpatrick J. D., Cutri R. M., Schneider S. E., Skrutskie M., van Driel W., 2000, *AJ*, **120**, 1876
- Ivanov V. D., Borissova J., Vanzi L., 2000, *A&A*, **362**, L1
- Ivanov V. D., Borissova J., Pessev P., Ivanov G. R., Kurtev R., 2002, *A&A*, **394**, L1
- King I., 1962, *AJ*, **67**, 471
- Madore B. F., et al., 2018, preprint, ([arXiv:1803.01278](https://arxiv.org/abs/1803.01278))
- Minniti D., 1995, *AJ*, **109**, 1663



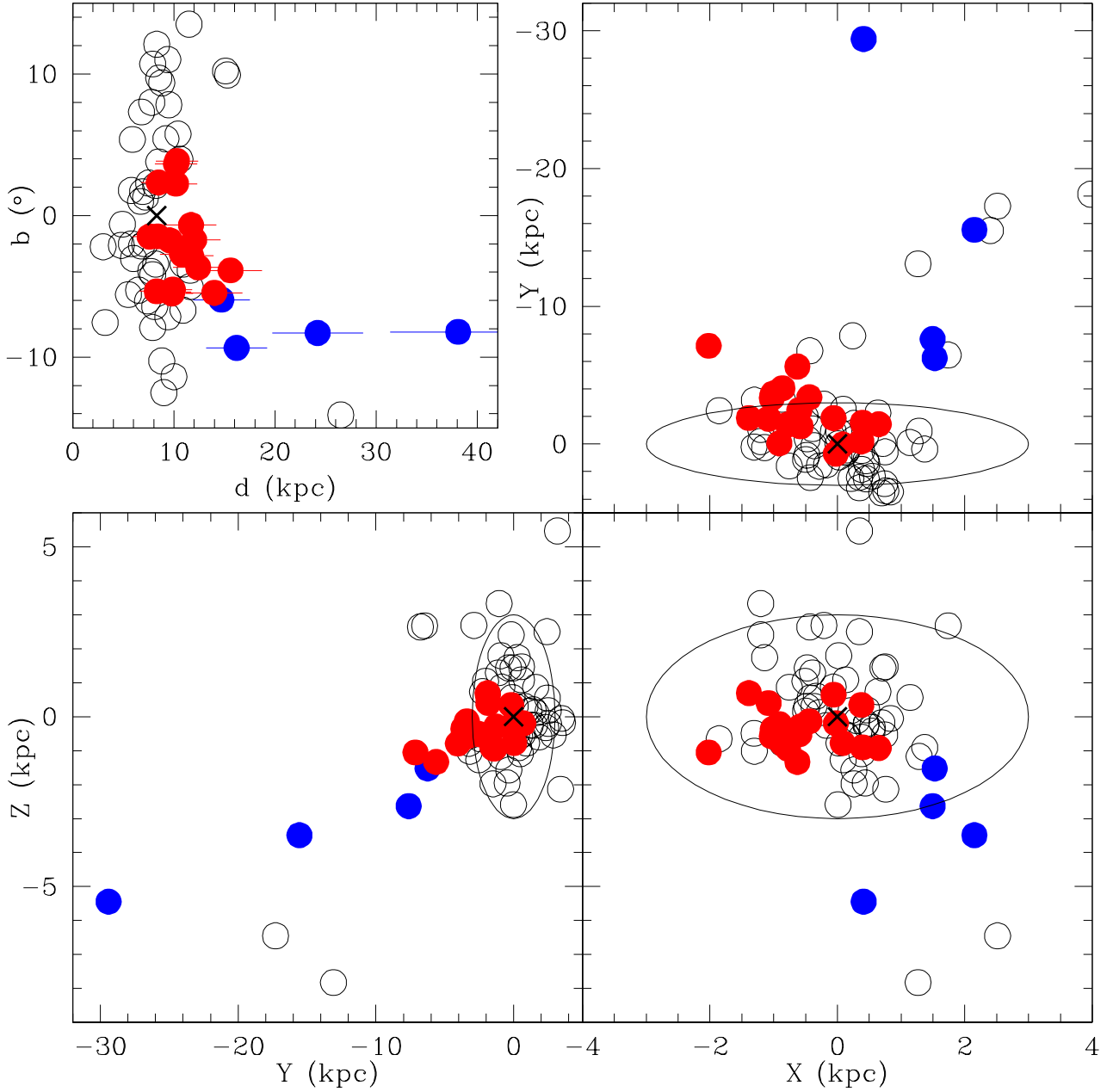


**Figure 5.** Spatial distribution of the studied GC candidates and those compiled by Harris (1996) for the same Galactic longitude interval drawn with filled and open circles, respectively. Red and blue filled circles correspond to GC candidates with metallicities smaller and larger than  $[\text{Fe}/\text{H}] = -0.8$  dex. A cross represents the position of the Galactic centre; while the Sun is located at  $(b,d) = (0,0)$  and  $(X,Y,Z)_{\odot} = (0,8.3,0)$ . A circle of radius 3 kpc is also shown.

Minniti D., et al., 2010, *New Astron.*, **15**, 433

Minniti D., et al., 2017, *ApJ*, **849**, L24

Müller O., Rejkuba M., Jerjen H., 2018, preprint, ([arXiv:1803.02406](https://arxiv.org/abs/1803.02406))

Piatti A. E., 2017, *ApJ*, **846**, L10

Piatti A. E., 2018, *MNRAS*, **473**, 492

Piatti A. E., Bica E., 2012, *MNRAS*, **425**, 3085

Piatti A. E., Cole A., 2017, *MNRAS*, **470**, L77

Piatti A. E., Cole A. A., Emptage B., 2018, *MNRAS*, **473**, 105

Plummer H. C., 1911, *MNRAS*, **71**, 460

Sabbi E., et al., 2018, preprint, ([arXiv:1801.05467](https://arxiv.org/abs/1801.05467))

Saito R. K., et al., 2012, *A&A*, **537**, A107

Scholz R.-D., Kharchenko N. V., Piskunov A. E., Röser S., Schilbach E., 2015, *A&A*, **581**, A39

Serenelli A., Weiss A., Cassisi S., Salaris M., Pietrinferni A., 2017, *A&A*, **606**, A33

Skrutskie M. F., et al., 2006, *AJ*, **131**, 1163

Strader J., Kobulnicky H. A., 2008, *AJ*, **136**, 2102

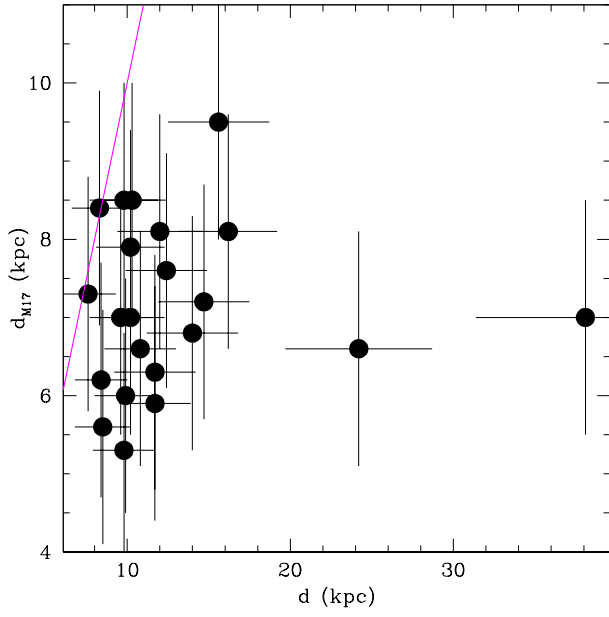


**Figure 6.** Comparison between heliocentric distances derived by M17 and in this work. The magenta line represents the identity relationship.

Valenti E., Ferraro F. R., Origlia L., 2004, [MNRAS](#), **351**, 1204  
 Vanderbeke J., De Propris R., De Rijcke S., Baes M., West M. J.,  
 Blakeslee J. P., 2015, [MNRAS](#), **450**, 2692  
 de Grijs R., Bono G., 2017, [ApJS](#), **232**, 22

This paper has been typeset from a  $\text{T}_{\text{E}}\text{X}/\text{L}^{\text{A}}\text{T}_{\text{E}}\text{X}$  file prepared by the author.

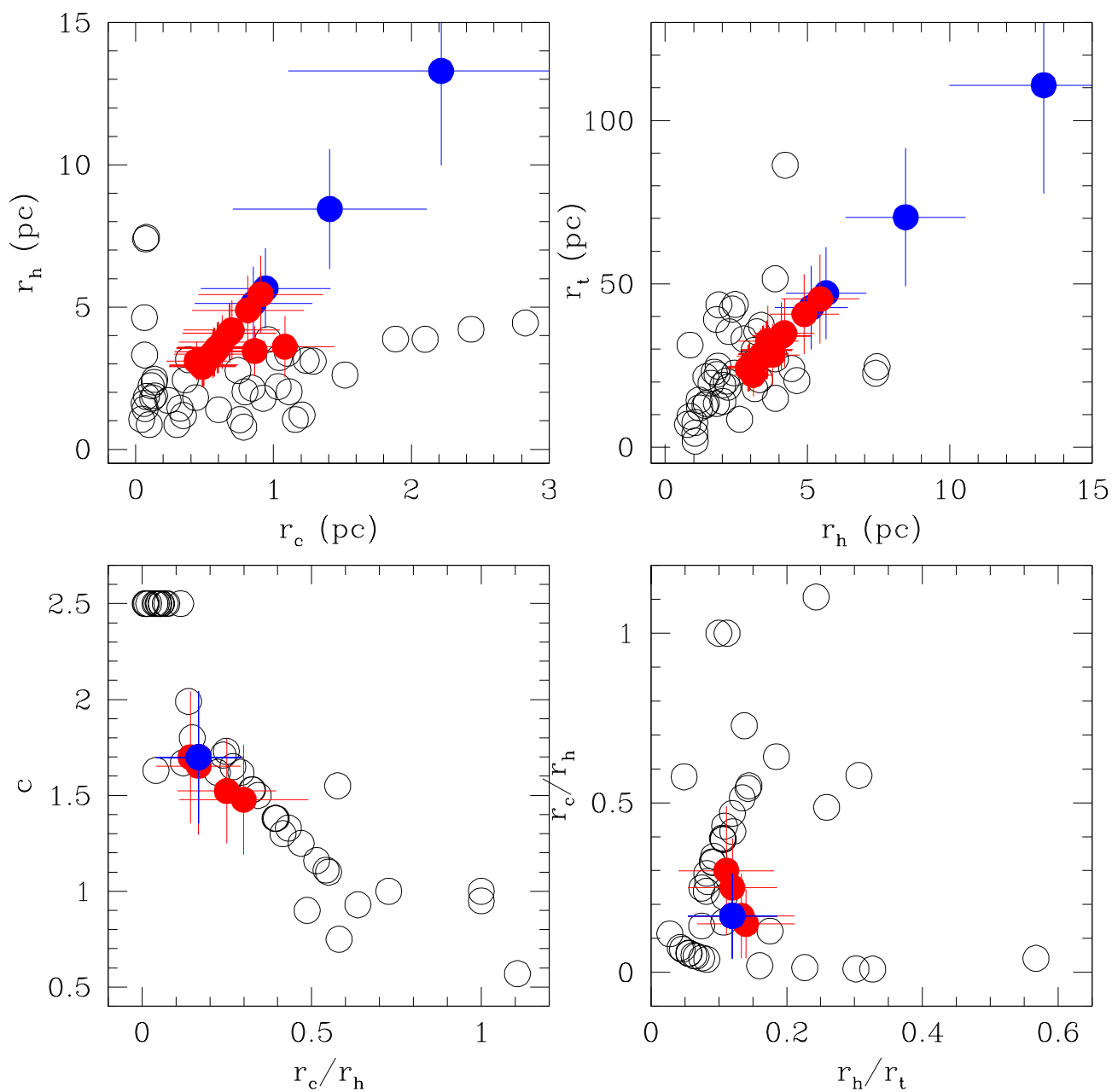


**Figure 7.** Relationships between different structural parameters with their respective errorbars. Symbols are as in Fig. 5.